$La_{0.6}Sr_{0.4}Co_{1-y}Fe_yO_{3-\delta}$ Perovskites: Influence of the Co/Fe Atomic Ratio on Properties and Catalytic Activity toward Alcohol Steam-Reforming

Marta Maria Natile,*[,†,‡] Fabio Poletto,[†] Alessandro Galenda,[†] Antonella Glisenti,[†,‡] Tiziano Montini,[§] Loredana De Rogatis,[§] and Paolo Fornasiero[§]

Dipartimento di Scienze Chimiche and INSTM-Padova, Università di Padova, via F. Marzolo 1, I-35131 Padova, Italy, and Dipartimento di Scienze Chimiche, Centro di Eccellenza per i Materiali Nanostrutturati, (CENMAT) and INSTM-Trieste, Università di Trieste, via L. Giorgieri 1, I-34127, Italy

Received November 22, 2007

$La_{0.6}Sr_{0.4}Co_{1-y}Fe_yO_{3-\delta}$ ($y = 0.2, 0.5, 0.8$) perovskite-type oxide powders were prepared by the citrate gel method with the aim of investigating the influence of cobalt/iron atomic ratio on the chemical and structural properties as well as on the catalytic activity. The samples were characterized by means of X-ray diffraction (XRD), X-ray photoelectron spectroscopy (XPS), thermal analysis, Kr physisorption surface area, scanning electron microscopy (SEM), and temperature programmed reduction (TPR). XRD outcomes reveal the formation of perovskite phase after calcination at 873 K. Depending on the Co/Fe atomic ratio, the perovskite exhibits two different structure: rhombohedral for $y < 0.5$, orthorhombic for $y \geq 0.5$. However, other phases are also observed. The crystallite size increases with the calcination temperature, while decreases with the iron content. The specific surface area of the $La_{0.6}Sr_{0.4}Co_{1-y}Fe_yO_{3-\delta}$ perovskites (calcined at 1073 K) is low, but increases with the iron amount: it varies between 4.1 and 6.6 $m^2\ g^{-1}$ moving from $y = 0.2$ to $y = 0.8$. XPS results reveal the presence of traces of Co(II) in the sample with lower cobalt amount. The scanning electron micrographs reveal nanoscaled near spherical particles which are clustered together, forming a highly porous microstructure. However, the samples with higher iron content show a more compact morphology due to the enhanced agglomeration. The perovskite phase is rather stable even after aggressive treatment as high temperature reduction. The influence of cobalt/iron atomic ratio on the catalytic activity toward alcohol steam reforming was investigated. All the samples present good alcohol dehydrogenation activity, as resulting from the methanol steam reforming experiments. In the steam reforming of ethanol, the $La_{0.6}Sr_{0.4}Co_{0.5}Fe_{0.5}O_{3-\delta}$ presents the better performance (especially after reduction at 873 K) with the complete conversion of ethanol into syngas above 850 K and the almost complete suppression of the ethylene formation at lower temperature. The differences of the activity toward ethanol steam reforming are attributable to a different stabilization of Co(0) nanoparticles produced during the reduction at 873 K.

Introduction

In a sustainable energy development, hydrogen, in combination with fuel cells, is considered to be one of the most promising energy vectors for the future. It could have an important role in order to substantially reduce the atmospheric pollution and the global dependency on fossil fuels, if produced from renewable resources.

Among different fuel cell technologies, solid oxide fuel cells (SOFCs) operating at high temperature (1100−1300 K) are considered as the most efficient and suitable source of electrical energy mainly for stationary applications. A reduction in working temperatures, however, could favor a widespread diffusion of SOFCs. A significant improvement of the properties of the existing anodes, cathodes, and electrolytes is therefore a fundamental step for the achievement of this goal.[1] An important characteristic of these fuel cells is the flexibility in the types of fuels they can utilize: carbonaceous fuels can be internally processed to obtain hydrogen without the need of an expensive external reformer.

Nowadays, catalytic steam reforming of alcohols is considered a technically feasible and convenient way to produce hydrogen. Methanol and ethanol are good candidate as a H_2 carrier, because they are a low-cost, virtually sulfur-free fluid with high energy density and are easier to store, handle, and transport in a safe way. Methanol is available as an abundant feedstock and already largely distributed. It is primarily produced from syngas, which may be derived from biomass (however, this process is not currently economically viable).[2] Ethanol, beside its lower toxicity, has the advantages that can be produced directly by fermentation of biomass, contributing to reduce carbon dioxide emissions.[2–5]

* Corresponding author. Tel.: 39 049 8275196. Fax: 39 049 8275161. E-mail: martamaria.natile@unipd.it.
† Dipartimento di Scienze Chimiche, Università di Padova.
‡ INSTM-Padova, Università di Padova.
§ Dipartimento di Scienze Chimiche, Centro di Eccellenza per i Materiali Nanostrutturati (CENMAT) and INSTM-Trieste, Università di Trieste.

(1) Park, S. D.; Vohs, J. M.; Gorte, R. J. *Nature* **2000**, *404*, 265.
(2) Palo, D. R.; Dangle, R. A.; Holladay, J. D. *Chem. Rev.* **2007**, *107*, 3992.
(3) Brown, L. F. *Int. J. Hydrogen Energy* **2001**, *26*, 381.
(4) Haryanto, A.; Fernando, S.; Murali, N.; Adhikari, S. *Energy Fuels* **2005**, *19*, 2098.

10.1021/cm703329k CCC: $40.75
Published on Web 02/27/2008

Beyond all doubt, catalytic technologies play a prominent role in the transition toward the hydrogen economy. The challenge lies in the development of catalysts with high catalytic activity and selectivity for hydrogen production as well as a good long-term stability.

Taking into account these considerations, we are exploring the possibility to develop oxide-based materials to be used as anode in intermediate temperature SOFCs (IT-SOFCs, $T \approx 900$ K).[6] In particular, our interest is in materials with mixed conductivity that can operate effectively using alcohol at intermediate temperatures with good and stable performance. The advantage of a mixed conducting material is that it may extend the available three phase boundary (gas/electrode/electrolyte) over the whole electrode surface.

Among the mixed metal oxides, perovskite-type oxides, ABO_3 (A = rare-earth, alkaline-earth metal and B = transition metal), result prominent.[7] These materials are very attractive for various kinds of industrial applications related to catalysis. They are commonly used as catalysts or supports for the flameless combustion of hydrocarbons,[8–10] the removal of volatile organic compounds,[11–14] or for the abatement of the pollutant emissions from engines.[15–18] Recently, perovskite-based materials have been tested as catalysts or precursors for the production of hydrogen through the reforming of methane[19–26] or higher hydrocarbons, such as diesel or jet fuel.[27–29] One of the interesting features of these complex mixed oxides is that their catalytic activity can be highly improved by partial substitution on A and/or B sites with only minimal changes in structure.[7] Moreover, perovskite materials also exhibit a variety of conductivity behaviors, ranging from predominantly electronic to almost purely ionic.

Recently, La−Sr−Co−Fe−O mixed oxides have attracted growing attention because of their superior mixed electronic−ionic conduction properties.[30–32] Moreover, they exhibit a significant oxygen permeability,[33] a good catalytic activity toward methane oxidation,[34–36] and chemical stability in the anodic conditions.[37]

In this study, $La_{0.6}Sr_{0.4}Co_{1-y}Fe_yO_{3-\delta}$ powders with y = 0.2, 0.5, and 0.8 were prepared by the citrate gel method. The Sr amount was chosen for its effect on the electrical properties.[31,32] A wet chemical preparation procedure was preferred to solid-state reaction between oxide and/or carbonate powder precursors because this method offers the possibility to obtain perovskite-type oxides at relatively lower temperature with very small grain size. All the prepared materials were deeply characterized by different techniques. Particular attention was paid to investigate the effect of the heat treatment on the final product and mainly the influence of Co/Fe ratio on the bulk (structure, morphology, crystallite and particle sizes) and the surface (specific surface area, surface chemical composition, and hydroxylation degree) properties of the prepared materials. The catalytic activity toward methanol and ethanol steam reforming was studied after different pretreatments and the results are discussed in connection to their properties. Although some work has been carried out on methane reforming on Fe/Co based perovskite,[21] to the best knowledge of the authors, no papers concerning La−Sr−Co−Fe−O compounds appear in the open literature dealing with the conversion of methanol and ethanol to hydrogen.

Experimental Section

(a) Synthesis. Three powders were prepared by the citrate gel method.[38–42] Appropriate amounts of $La(NO_3)_3 \cdot 6H_2O$ (Aldrich, 99.999%), $Sr(NO_3)_2$ (Carlo Erba, >98%), $Co(NO_3)_2 \cdot 6H_2O$ (Acros, 99%), and $Fe(NO_3)_3 \cdot 9H_2O$ (Janssen, 99%) were carefully weighed and dissolved in deionized water. Citric acid (Acros, 99.5%) was added as complexing agent to the above solution. The amount of

(5) Hickey, N.; Fornasiero, P.; Graziani, M. Hydrogen Based Technologies for Mobile Applications. In *Renewable Resources and Renewable Energy: A Global Challenge*; Graziani, M., Fornasiero; P., Eds.; Taylor & Francis: New York. 2006; Chapter 11, pp 225–272..
(6) Haile, S. M. *Acta Mater.* **2003**, *51*, 5981.
(7) Peña, M. A.; Fierro, J. L. G. *Chem. Rev.,* **2000**, *101*, 1381.
(8) Leanza, R.; Rossetti, I.; Fabbrini, L.; Oliva, C.; Forni, L. *Appl. Catal., B* **2000**, *28*, 55.
(9) Forni, L.; Rossetti, I. *Appl. Catal., B* **2002**, *38*, 29.
(10) Oliva, C.; Bonoldi, L.; Cappelli, S.; Fabbrini, L.; Rossetti, I.; Forni, L. *J. Mol. Catal. A:Chem.* **2005**, *226*, 33.
(11) Sinquin, G.; Petit, C.; Hindermann, J. P.; Kiennemann, A. *Catal. Today* **2001**, *70*, 183.
(12) Blasin-Aubé, V.; Belkouch, J.; Monceaux, L. *Appl. Catal., B* **2003**, *43*, 175.
(13) Barbero, B. P.; Gamboa, J. A.; Cadus, L. E. *Appl. Catal., B* **2006**, *65*, 21.
(14) Niu, J.; Deng, J.; Liu, W.; Zhang, L.; Wang, G.; Dai, H.; He, H.; Zi, X. *Catal. Today* **2007**, *126*, 420.
(15) Zhang, R.; Villanueva, A.; Alamdari, H.; Kaliaguine, S. *Appl. Catal., B* **2006**, *64*, 220.
(16) Li, X.; Chen, J.; Lin, P.; Meng, M.; Fu, Y.; Tu, J.; Li, Q. *Catal. Commun.* **2004**, *5*, 25.
(17) Peng, X.; Lin, H.; Shangguan, W.; Huang, Z. *Ind. Eng. Chem. Res.* **2006**, *45*, 8822.
(18) Belessi, V. C.; Costa, C. N.; Bakas, T. V.; Anastasiadou, T.; Pomonis, P. J.; Efstathiou, A. M. *Catal. Today* **2000**, *59*, 347.
(19) Guo, J.; Lou, H.; Zhu, Y.; Zheng, X. *Mater. Lett.* **2003**, *57*, 4450.
(20) Sauvet, A. L.; Irvine, J. T. S. *Solid State Ionics* **2004**, *167*, 1.
(21) Goldwasser, M. R.; Rivas, M. E.; Lugo, M. L.; Pietri, E.; Pérez-Zurita, J.; Cubeiro, M. L.; Griboval-Constant, A.; Leclercq, G. *Catal. Today* **2005**, *107* (108), 106.
(22) Batiot-Dupeyrat, C.; Gallego, G. A. S.; Mondragón, F.; Barrault, J.; Tatibouët, J.-M. *Catal. Today* **2005**, *107* (108), 474.
(23) Gonzalez, O.; Lujano, J.; Pietri, E.; Goldwasser, M. R. *Catal. Today* **2005**, *107* (108), 436.
(24) de Lima, S. M.; Assaf, J. M. *Catal. Lett.* **2006**, *108*, 63.
(25) Lima, S. M.; Assaf, J. M.; Peña, M. A.; Fierro, J. L. G. *Appl. Catal., A* **2006**, *311*, 94.
(26) Choudhary, V. R.; Mondal, K. C. *Appl. Energy* **2006**, *83*, 1024.
(27) Qi, A.; Wang, S.; Fu, G.; Ni, C.; Wu, D. *Appl. Catal., A* **2005**, *281*, 233.
(28) Liu, D.-J.; Krumpelt, M. *Int. J. Appl. Ceram. Technol.* **2005**, *2*, 301.
(29) Erri, P.; Dinka, P.; Varma, A. *Chem. Eng. Sci.* **2006**, *61*, 5328.
(30) Tai, L.-W.; Nasrallah, M. M.; Anderson, H. U.; Sparlin, D. M.; Sehlin, S. R. *Solid State Ionics* **1995**, *76*, 259.
(31) Tai, L.-W.; Nasrallah, M. M.; Anderson, H. U.; Sparlin, D. M.; Sehlin, S. R. *Solid State Ionics* **1995**, *76*, 273.
(32) Mineshige, A.; Izutsu, J.; Nakamura, M.; Nigaki, K.; Abe, J.; Kobune, M.; Satoshi, F.; Yazawa, T. *Solid State Ionics* **2005**, *176*, 1145.
(33) Teraoka, Y.; Zhang, H.-M.; Furukawa, S.; Yamazoe, N. *Chem. Lett.* **1985**, 1743.
(34) Balachandran, U.; Dusek, J. T.; Mieville, R. L.; Poeppel, R. B.; Kleefisch, M. S.; Pei, S.; Kobylinski, T. P.; Udovich, C. A.; Bose, A. C. *Appl. Catal., A* **1995**, *133*, 19.
(35) Weston, M.; Metcalfe, I. S. *Solid State Ionics* **1998**, *113–115*, 247.
(36) Hartley, A.; Sahibzada, M.; Weston, M.; Metcalfe, I. S.; Mantzavinos, D. *Catal. Today* **2000**, *55*, 197.
(37) Xu, S. J.; Thomson, W. J. *Ind. Eng. Chem. Res.* **1998**, *37*, 1290.
(38) Taguchi, H.; Yamada, S.; Nagao, M.; Ichikawa, Y.; Tabata, K. *Mater. Res. Bull.* **2002**, *37*, 69.
(39) Zhang, H. M.; Teraoka, Y.; Yamazoe, N. *Chem. Lett.* **1987**, 665.
(40) Ferri, D.; Forni, L. *Appl. Catal., B* **1998**, *16*, 119.
(41) Ciambelli, P.; Cimino, S.; Lisi, L.; Faticanti, M.; Minelli, G.; Pettiti, I.; Porta, P. *Appl. Catal., B* **2001**, *33*, 193.
(42) Ciambelli, P.; Cimino, S.; De Rossi, S.; Lisi, L.; Minelli, G.; Porta, P.; Russo, G. *Appl. Catal., B* **2001**, *29*, 239.

citric acid was such that the ratio between the total moles of cations to that of citric acid was 1:1. The resulted aqueous solution was slowly evaporated under slow stirring at about 343 K until a gel was obtained. The viscous gel was dried at 383 K. The obtained spongy material was finely ground and calcined at 873 K for 5 h and then at 1073 K for 5 h (in air).

(b) Characterization. X-ray diffraction (XRD) patterns were obtained with a Bruker D8 Advance diffractometer with Bragg–Brentano geometry operating at 40 kV and 40 mA with a Cu Kα radiation ($\lambda = 0.154$ nm). The data were collected at 0.02° at a counting time of 10 s per step in the (2θ) range from 20° to 80°. The various crystalline phases were identified by the search-match method using the JCPDS database. The phase compositions, structure, lattice parameters, and crystallite sizes of the powders were determined with great accuracy by Rietveld's powder structure refinement analysis of XRD data, by using the MAUD (Material Analysis Using Diffraction) software.[43] It applies the RITA/RISTA method as developed by Wenk et al.[44] and Ferrari and Lutterotti.[45] The Rietveld's method has given a reasonable fit of the diffraction profiles ($R_{wp} \leq 5\%$). The required crystallographic data were taken from ICSD (Inorganic Crystal Structure Database, version 2007, Fachinformationszentrum, Karlsruhe, Germany).

XP spectra were recorded by using a Perkin-Elmer PHI 5600 ci spectrometer with a standard Mg Kα source (1253.6 eV) working at 400 W. The working pressure was less than 7×10^{-7} Pa. The spectrometer was calibrated by assuming the binding energy (BE) of the Au $4f_{7/2}$ line to be 84.0 eV with respect to the Fermi level. Extended spectra (survey) were collected in the range 0 - 1150 eV (187.85 eV pass energy, 0.5 eV step, 0.025 s.step^{-1}). Detailed spectra were recorded for the following regions: La 3d, Sr 3d, Co 2p, Fe 2p, O 1s, and C 1s, (11.75 eV pass energy, 0.1 eV step, 0.1 s.step^{-1}). The standard deviation in the BE values of the XPS line is 0.10 eV. The atomic percentage, after a Shirley type background subtraction,[46] was evaluated by using the PHI sensitivity factors.[47] To take into account charging problems the C 1s peak was considered at 285.0 eV and the peaks BE differences were evaluated. The sample for the XPS analysis was processed as a pellet by pressing the powder at ca. 6×10^8 Pa for 10 min; the pellet was then evacuated for 12 h at ca. 1×10^{-3} Pa.

Thermogravimetric analysis (TGA) was carried out in a controlled atmosphere using the Simultaneous Differential Techniques (SDT) 2960 of TA Instruments. Thermograms were recorded at 15 K min^{-1} heating rate in air and in nitrogen flow. The covered temperature ranged from room temperature (RT) to 1273 K.

Field-emission scanning electron microscopy (FE-SEM) and energy-dispersive X-ray analysis (EDX) were run on a Zeiss SUPRA 40VP equipped with an Oxford INCA x-sight X-ray detector. Morphological analysis was carried out setting the acceleration voltages between 1.00 kV and 10 kV without significant differences, whereas the EDX compositional investigations were obtained setting the acceleration voltage at 10 kV.

BET surface areas were measured by Kr physisorption at liquid nitrogen temperature using a Micromeritics ASAP 2020 apparatus. The samples were degassed at 623 K for 12 h before analysis.

Temperature-programmed reductions (TPR) were performed using 20 mg of the materials calcined at 1073 K. The samples were pretreated at 773 K for 1 h with pulses of O_2 (100 μL) in a flow of Ar (25 mL min^{-1}), then cooled to RT. The O_2 pulses were stopped when the sample temperature was lower than 423 K. H_2 (5%)/Ar flow (25 mL min^{-1}) was admitted to the reactor and the flow allowed to stabilize for 30 min before increasing the temperature to 1273 K (10 K min^{-1}). During the heating ramp, hydrogen consumption was monitored using a thermal conductivity detector (TCD).

(c) Catalytic Activity. Catalytic experiments were conducted in a U-shaped 4 mm ID quartz microreactor. Typically, 12 mg of pelletized catalyst (∼2 tonn cm^{-2}, 250−300 μm), diluted in a 1:2 weight ratio with high-purity Al_2O_3 (Grace Davison, calcined at 1573 K for 15 h) were used. Liquid mixtures were injected into an Ar flow with a Hamilton Gastight syringe using a INSTECH Model 2000 syringe pump. All the transfer lines between syringe, reactor and gas-chromatograph (GC) were heated to 393 K. As reagents, aqueous solution of methanol and ethanol were used with a 1:4 and 1:5 molar ratio respectively. Gas flow rates of ∼40 mL min^{-1} (GHSV ∼200000 mL g^{-1} h^{-1}) were used in the case of methanol steam reforming and gas flow rates of ∼30 mL min^{-1} (GHSV values of ∼150 000 mL g^{-1} h^{-1}) were used in the case of ethanol steam reforming.

Online GC analysis was performed using a Hewlett-Packard 5890 Series II gas chromatograph. A Molsieve 5A column, with Ar as carrier, was connected to a TCD to analyze H_2, O_2, N_2, CH_4, and CO. A PoraPLOT Q column, with He as carrier, was connected in series to a methanator and to a flame ionization detector (FID) to analyze the carbon-containing compounds. C balance was always within ±2%.

Before testing the catalytic activity, the calcined materials were cleaned under O_2 (5%)/Ar at 773 K for 1 h (40 mL min^{-1}, 10 K min^{-1}). When necessary, a reduction in flowing H_2 (5%)/Ar at the desired temperature (873 or 1273 K) for 2 h was also done. The gaseous mixture was first introduced in the reactor at 423 K for 1 h, before ramping the furnace temperature to 973 at 1 K min^{-1}. After 2 h at 973 K, the furnace was cooled to 423 K at the same rate. All the results of the catalytic activity are reported as number of moles of each compound with respect to the initial number of moles of alcohol.

Results and Discussion

(a) Characterization. The XRD patterns of the $La_{0.6}Sr_{0.4}Co_{1-y}Fe_yO_{3-\delta}$ samples as a function of the thermal treatment are shown in Figure 1. XRD analysis indicates that the perovskite-type structure is always the main phase and it is observed since 873 K. This result indicates that the citrate gel method allows to obtain the desired $La_{0.6}Sr_{0.4}Co_{1-y}Fe_yO_{3-\delta}$ crystalline phase at significantly lower temperature (873 K) than that required by the Pechini method (1173 K).[48] Reflections characteristic of other phases are also evident. The $SrCO_3$ phase is present in the diffraction patterns of all the samples; it is the most abundant secondary compound. $SrLaCoO_4$ and Co_3O_4 phases are also observed on the patterns of the samples with $y = 0.2$ and 0.5, whereas small amounts of $SrLaFeO_4$ and Fe_2O_3 are detected in addition to the perovskite and strontium carbonate phases when $y = 0.8$. However, due to the detection limits of the XRD technique and the overlapping of the reflections, the segregation of other phases (such as lanthanum oxide) cannot be completely excluded. From the refinement of XRD patterns,

(43) http://www.ing.unitn.it/∼luttero/maud/.
(44) Wenk, H. R.; Matthies, S.; Lutterotti, L. *Mater. Sci. Forum* **1994**, *157* (162), 473.
(45) Ferrari, M.; Lutterotti, L. *J. Appl. Phys.* **1994**, *76*, 7246.
(46) Shirley, D. A. *Phys. Rev. B* **1972**, *5*, 4709.
(47) Moulder, J. F.; Stickle, W. F.; Sobol, P. E.; Bomben, K. D. In *Handbook of X-ray Photoelectron Spectroscopy*; Chastain, J., Ed.; Physical Electronics: Eden Prairie, MN, 1992.
(48) Galenda, A.; Natile, M. M.; Krishnan, V.; Bertagnolli, H.; Glisenti, A. *Chem. Mater.* **2007**, *19*, 2796.

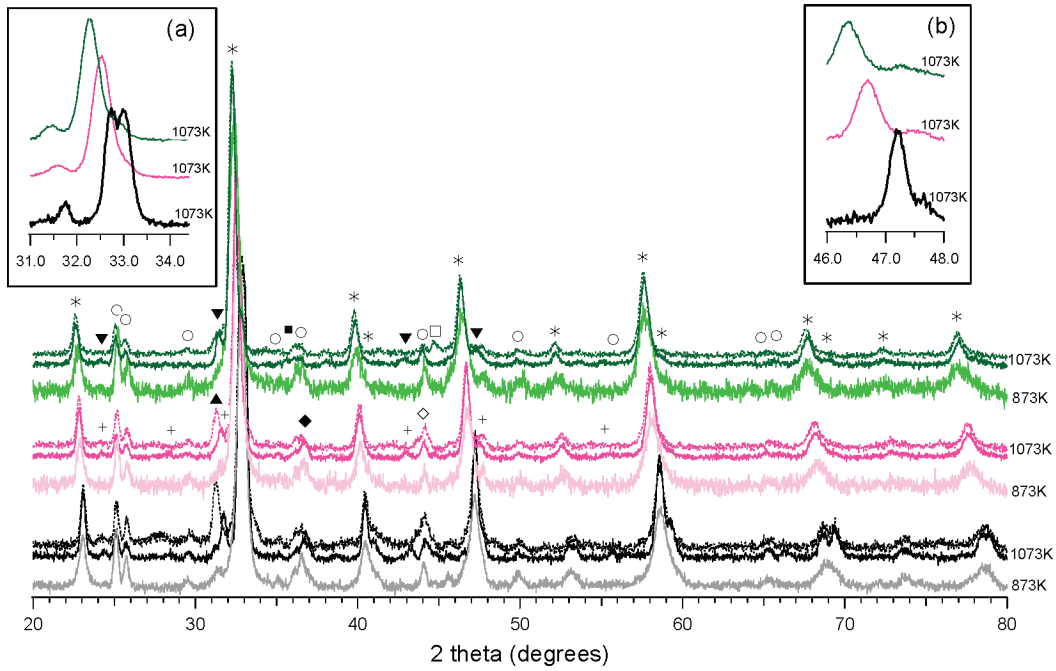

Figure 1. XRD patterns obtained for the three $La_{0.6}Sr_{0.4}Co_{1-y}Fe_yO_{3-\delta}$ samples prepared by citrate gel method and treated at 873 K (light color) and at 1073 K (dark color) before (solid line) and after (dotted line) H_2-TPR experiments: (black) $La_{0.6}Sr_{0.4}Co_{0.8}Fe_{0.2}O_{3-\delta}$; (magenta) $La_{0.6}Sr_{0.4}Co_{0.5}Fe_{0.5}O_{3-\delta}$; (green) $La_{0.6}Sr_{0.4}Co_{0.2}Fe_{0.8}O_{3-\delta}$; perovskite (*); $SrCO_3$ (○); $SrLaCoO_4$ (+); Co_3O_4 (♦); $SrLaFeO_4$ (▼); Fe_2O_3 (■); La_2CoO_4 (▲); metallic cobalt (◊); metallic iron (□).

Table 1. Results of Quantitative Phase Analysis (given in wt %) of all the $La_{0.6}Sr_{0.4}Co_{1-y}Fe_yO_{3-\delta}$ Powders Treated at 873 K and at 1073 K before and after H_2-TPR Experiment, Respectively (values normalized with respect to perovskite are reported in parentheses)

sample	thermal treatment	$La_{0.6}Sr_{0.4}Co_{1-y}Fe_yO_3$	$SrCO_3$	$SrLaCoO_4$	Co_3O_4	$SrLaFeO_4$	Fe_2O_3	La_2CoO_4	Co hcp	Co ccp	Fe
$La_{0.6}Sr_{0.4}Co_{0.8}Fe_{0.2}O_{3-\delta}$	873 K	62 (1)	21 (0.339)	5 (0.081)	12 (0.194)						
	1073 K	66 (1)	12 (0.182)	11 (0.167)	11 (0.167)						
	1073 K, H_2-TPR	61 (1)	19 (0.311)	5 (0.082)				9 (0.148)	2 (0.033)	4 (0.066)	
$La_{0.6}Sr_{0.4}Co_{0.5}Fe_{0.5}O_{3-\delta}$	873 K	67 (1)	22 (0.328)	3 (0.045)	8 (0.119)						
	1073 K	67 (1)	14 (0.209)	9 (0.134)	10 (0.149)						
	1073 K, H_2-TPR	67 (1)	21 (0.313)					9 (0.134)		3 (0.045)	
$La_{0.6}Sr_{0.4}Co_{0.2}Fe_{0.8}O_{3-\delta}$	873 K	69 (1)	26 (0.377))			5 (0.072)					
	1073 K	66 (1)	15 (0.227)			10 (0.152)	9 (0.136)				
	1073 K, H_2-TPR	72 (1)	21 (0.292)			4 (0.056)					3 (0.042)

by means of Rietveld's method, the weight fractions of the different phases were obtained and the results are shown in Table 1.

After the heat treatment at 1073 K for 5 h, the contributions due to $SrCO_3$ decrease. This behavior suggests that strontium diffuses into perovskite structure at high temperature. On the contrary, with increasing of the calcination temperature the reflections characteristic of the $SrLaCoO_4$-type and $SrLaFeO_4$-type species, which have a body-centered tetragonal K_2NiF_4-type structure consisting of alternating layers of ABO_3 perovskite and AO rock salt along *c*-axis,[49,50] become more intense on the samples with $y = 0.2$, 0.5 and $y = 0.8$, respectively. Also the contributions characteristic of Co_3O_4 (for the samples with $y = 0.2$ and 0.5) and Fe_2O_3 (for the sample with $y = 0.8$) slightly increase.

A detailed analysis of the XRD patterns of the $La_{0.6}Sr_{0.4}Co_{1-y}Fe_yO_{3-\delta}$ perovskite series leads to other relevant observations. It is worth underline that with increasing of iron content a notable shift of the diffraction lines of the perovskite phase toward lower angles (see inserts in Figure 1) as well as a change of peak shape are observed. The crystalline structure has to be considered to explain the peak shape variation. $LaCoO_3$ and $LaFeO_3$ reference perovskites, in fact, have rhombohedral and orthorhombic structure respectively, which only differ by the distortion of the iron coordination octahedral alignment compared to cobalt. Differentiation between the two structures is simple and can be done by analyzing the main diffraction line. This line is a doublet in the rhombohedral structure and a single signal in the orthorhombic one. This change is well evident when the XRD patterns of the samples calcined at 1073 K are considered. As shown in detail (a) of Figure 1, the most intense diffraction line (at 2θ between 32−34°) is a doublet for the sample $La_{0.6}Sr_{0.4}Co_{0.8}Fe_{0.2}O_{3-\delta}$, whereas it is single for the samples with $y = 0.5$, 0.8. The substitution of iron for cobalt then leads to structural changes. This observation is in agreement with findings of Bebel et al.[51] Moreover, the structure refinement by Rietveld's method is very satisfactory when considering a rhombohedral symmetry for $La_{0.6}Sr_{0.4}Co_{0.8}Fe_{0.2}O_{3-\delta}$, and an orthorhombic one for the samples

(49) Castro-García, S.; Sánchez-Andújar, M.; Rey-Cabezudo, C.; Señarís-Rodríguez, M. A.; Julien, C. *J. Alloys Compd.* **2001**, *324* (324), 710.
(50) Jennings, A. J.; Skinner, S. J. *Solid State Ionics* **2002**, *152* (153), 663.
(51) Bebel, L.; Roger, A. C.; Estournes, C.; Kiennemann, A. *Catal. Today* **2003**, *85*, 207.

Table 2. Structure, Unit-Cell Parameters, Crystallite Sizes, and the Reliability Factor (R_{wp}) of $La_{0.6}Sr_{0.4}Co_{1-y}Fe_yO_{3-\delta}$ powders treated at 873 K and at 1073 K before and after H_2-TPR Experiment Respectively, from Rietveld's Method (the error values are reported in parentheses)

samples	thermal treatment	crystallographic system	lattice parameters (Å)			crystallite size (Å)	R_{wp} (%)
			a	*b*	*c*		
$La_{0.6}Sr_{0.4}Co_{0.8}Fe_{0.2}O_{3-\delta}$	873 K	rhombohedral	5.460 (0.001)		13.233 (0.002)	306 (7)	1.66
	1073 K	rhombohedral	5.460 (0.001)		13.200 (0.001)	692 (17)	1.88
	1073 K, H_2-TPR	rhombohedral	5.464 (0.001)		13.208 (0.001)	492 (13)	1.85
$La_{0.6}Sr_{0.4}Co_{0.5}Fe_{0.5}O_{3-\delta}$	873 K	orthorhombic	5.468 (0.003)	5.522 (0.003)	7.759 (0.006)	262 (7)	3.78
	1073 K	orthorhombic	5.468 (0.001)	5.515 (0.001)	7.779 (0.001)	509 (9)	2.17
	1073 K, H_2-TPR	orthorhombic	5.475 (0.001)	5.515 (0.001)	7.781 (0.002)	483 (5)	2.21
$La_{0.6}Sr_{0.4}Co_{0.2}Fe_{0.8}O_{3-\delta}$	873 K	orthorhombic	5.499 (0.003)	5.555 (0.003)	7.839 (0.005)	211 (4)	4.26
	1073 K	orthorhombic	5.499 (0.001)	5.537 (0.001)	7.828 (0.001)	438 (7)	2.72
	1073 K, H_2-TPR	orthorhombic	5.510 (0.002)	5.538 (0.001)	7.831 (0.002)	375 (5)	2.52

Table 3. XPS Peak Positions (Binding Energy, eV) Obtained for All the $La_{0.6}Sr_{0.4}Co_{1-y}Fe_yO_{3-\delta}$ Powders Treated at 873 and 1073 K, Respectively

	$La_{0.6}Sr_{0.4}Co_{0.8}Fe_{0.2}O_{3-\delta}$		$La_{0.6}Sr_{0.4}Co_{0.5}Fe_{0.5}O_{3-\delta}$		$La_{0.6}Sr_{0.4}Co_{0.2}Fe_{0.8}O_{3-\delta}$	
XPS peaks	873 K	1073 K	873 K	1073 K	873 K	1073 K
$La3d_{5/2}$	834.0	833.9	833.9	833.9	834.1	833.8
	837.9	837.8	837.9	837.8	838.1	837.9
$La3d_{3/2}$	850.8	850.7	850.7	850.7	850.9	850.6
	854.7	854.7	854.8	854.8	855.0	854.8
$Sr3d_{5/2}$	132.1	131.8	132.1	131.8	132.0	131.8
	133.6	133.3	133.7	133.3	133.6	133.2
	135.2	134.6	135.7	134.2	135.8	133.8
$Co2p_{3/2}$	780.2	780.2	780.2	780.3	780.2	780.5
$Co2p_{1/2}$	795.7	795.7	795.6	795.7	795.6	795.6
$Fe2p_{3/2}$	710.8	710.8	710.6	710.5	710.6	710.6
$Fe2p_{1/2}$	724.2	724.1	724.0	724.1	724.1	724.1
O 1s	528.8	528.9	528.8	528.7	529.0	528.7
	529.3	529.4	529.4	529.4	529.6	529.6
	531.4	531.4	531.5	531.4	531.5	531.4
	532.8	533.0	533.0	532.1	532.5	532.1
					533.9	

with $y = 0.5, 0.8$. The shift of the diffraction lines of the perovskite toward lower 2θ angles is linearly correlated with the iron content. This behavior implies that the unit cell parameters increase with the increase of y and thus with interchanging cobalt and iron ions. The Fe(III) ions, in fact, are characterized by a ionic radii slightly greater (0.645 Å) than Co(III) ions (0.61 Å).[52] The increment of the unit cell parameters is also corroborated by structure refinement obtained using the Rietveld's method, as listed in Table 2.

The crystallite sizes are reported in Table 2. As the treatment temperature is raised, an increase of the crystallite sizes is observed. This is particularly evident on the sample $La_{0.6}Sr_{0.4}Co_{0.8}Fe_{0.2}O_{3-\delta}$. This means that an appreciable crystallite growth occurs during the thermal treatment. Moreover, it is important to note that the values of crystallite sizes decrease with increasing of iron amount.

Interesting information concerning the surface properties (composition and chemical state) of the prepared powders derives from the XPS analysis. Also, in this case, the surface evolution was investigated as a function of the thermal treatment as well as of the composition.

The XP extended spectra (survey) do not reveal the presence of species different from the expected ones (i.e., La, Sr, Co, Fe, O, C). The binding energies of the XP peaks for the $La_{0.6}Sr_{0.4}Co_{1-y}Fe_yO_{3-\delta}$ powders measured in this work are summarized in Table 3.

The La 3d level (Figure 2, Table 3) is characterized by a double peak for each spin–orbit component, attributed either to energy loss phenomena ("shake-up" satellites) induced by intense O 2p → La 4f charge transfer events[53] or to strong final state mixing of electronic configurations.[54] La 3d peak positions (around 833.9 and 850.7 eV for La $3d_{5/2}$ and $3d_{3/2}$, respectively) and shape observed for all the samples agree with the values reported in literature for similar perovskites.[55,56] Only for the $La_{0.6}Sr_{0.4}Co_{0.2}Fe_{0.8}O_{3-\delta}$ sample treated at 873 K the slightly higher binding energy of the La 3d peak (Table 3) also suggests the presence of traces of La(III) oxide or hydroxide.[57–60]

The Co 2p XP spectra (Figure 2, Table 3) are similar in shape and the core level binding energies do not significantly change with the thermal treatment and with the cobalt/iron atomic ratio. The Co 2p peak shape and the positions observed for Co $2p_{3/2}$ and $2p_{1/2}$, respectively, are characteristic of the low spin Co(III) compounds.[55,61] However, in the spectra of the samples characterized by lower amount of cobalt, the presence of the shake-up peaks around 787.2 and 803.1 eV (indicated by arrows in the

(52) Shannon, R. D. *Acta Crystallogr., Sect. A* **1976**, *32*, 751.
(53) Burroughs, P.; Hamnett, A.; Orchard, A. F.; Thornton, G. *J. Chem. Soc., Dalton Trans.* **1976**, *17*, 1686.
(54) Vasquez, R. P. *Phys. Rev. B* **1996**, *54*, 14938.
(55) Machova, M.; Braskova, N.; Ivanov, P.; Carda, J. B.; Kozhukharov, V. *Appl. Surf. Sci.* **1997**, *119*, 127.
(56) van der Heide, P. A. W. *Surf. Interface Anal.* **2002**, *33*, 414.
(57) Natile, M. M.; Ugel, E.; Maccato, C.; Glisenti, A. *Appl. Catal., B* **2007**, *72*, 351.
(58) *Nist XPS Database 20, Version 3.4 (Web Version)*.
(59) Uwamino, Y.; Ishizuka, T.; Yamatera, H. *J. Electron Spectrosc. Relat. Phenom.* **1984**, *34*, 67.
(60) Barr, T. L. *J. Phys. Chem.* **1978**, *82*, 1801.
(61) Natile, M. M.; Glisenti, A. *Chem. Mater.* **2002**, *14*, 3090.

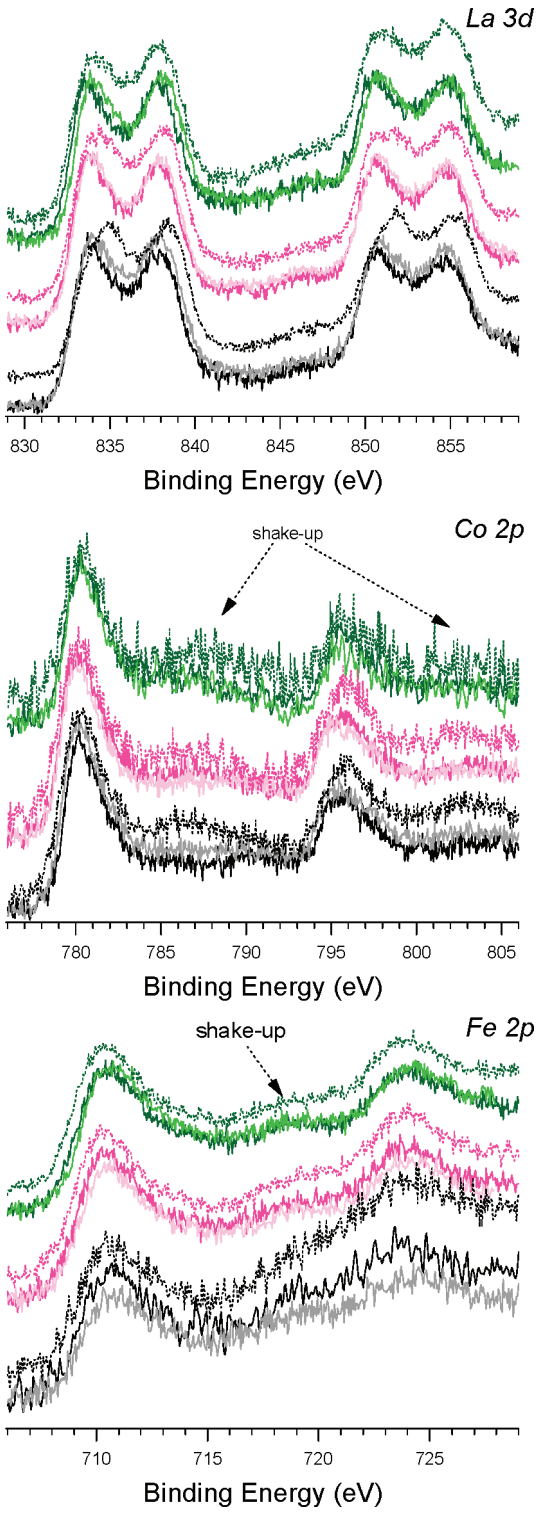

Figure 2. La 3d, Co 2p, and Fe 2p XP spectra of the three $La_{0.6}Sr_{0.4}Co_{1-y}Fe_yO_{3-\delta}$ samples prepared by citrate gel method and treated at 873 K (light color) and at 1073 K (dark color) before (solid line) and after H_2-TPR experiments (dotted line): (black) $La_{0.6}Sr_{0.4}Co_{0.8}Fe_{0.2}O_{3-\delta}$; (magenta) $La_{0.6}Sr_{0.4}Co_{0.5}Fe_{0.5}O_{3-\delta}$; (green) $La_{0.6}Sr_{0.4}Co_{0.2}Fe_{0.8}O_{3-\delta}$. (The spectra are normalized with respect to their maximum value).

(62) Co(II) and Co(III) compounds can be differentiated in XPS using their different magnetic properties. As a matter of fact, the XP spectra of Co(II) high spin compounds are characterized by an intense shake-up satellite structure around 787.0 and 804.0 eV. Unlike Co(II) compounds, in the low spin Co(III) compounds the satellite structure is weak or missing. See as an example: McIntyre, N. S.; Cook, M. G. *Anal. Chem.* **1975**, *47*, 2208.

(63) Seim, H.; Nieminen, M.; Niinistö, L.; Fjellvåg, H.; Johansson, L. S. *Appl. Surf. Sci.* **1997**, *112*, 243.

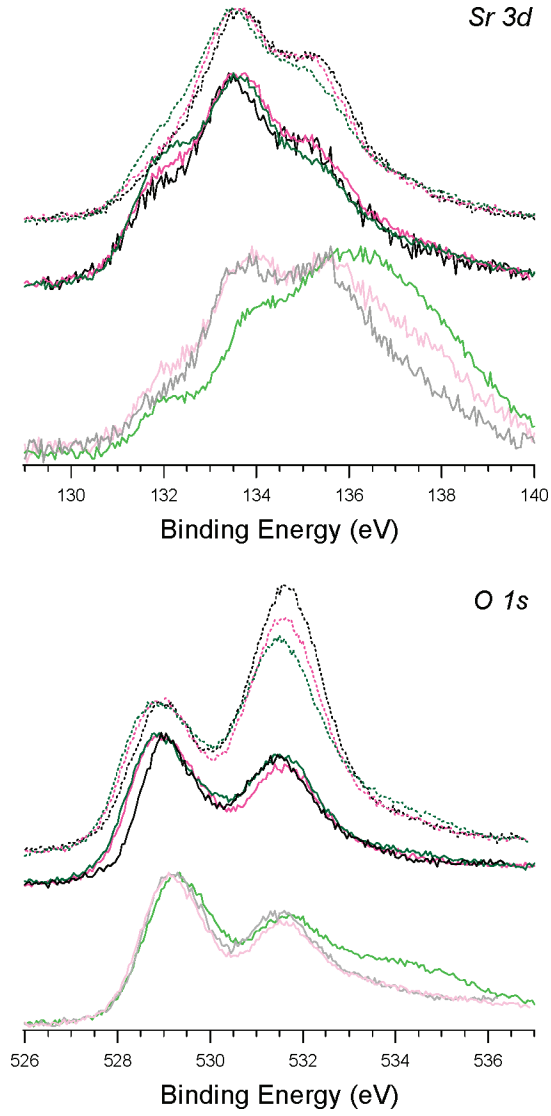

Figure 3. Sr 3d and O 1s XP spectra of the three $La_{0.6}Sr_{0.4}Co_{1-y}Fe_yO_{3-\delta}$ samples prepared by citrate gel method and treated at 873 K (light color) and at 1073 K (dark color) before (solid line) and after (dotted line) H_2-TPR experiments: (black) $La_{0.6}Sr_{0.4}Co_{0.8}Fe_{0.2}O_{3-\delta}$; (magenta) $La_{0.6}Sr_{0.4}Co_{0.5}Fe_{0.5}O_{3-\delta}$; (green) $La_{0.6}Sr_{0.4}Co_{0.2}Fe_{0.8}O_{3-\delta}$. (The spectra are normalized with respect to their maximum value).

Figure 2) also testifies the existence of Co(II).[62] The experimental Co $2p_{3/2}$–Co $2p_{1/2}$ energy splitting (~15.3 eV) is in good agreement with the literature data for Co-containing perovskite.[63]

The Fe 2p peak shape and the binding energies do not change with the thermal treatment or with the cobalt/iron atomic ratio (Figure 2, Table 3). The peak positions (around 710.5–710.8 and 724.0–724.2 eV for Fe $2p_{3/2}$ and $2p_{1/2}$, respectively) and the shake-up contribution at about 718.6 eV are consistent with the presence of Fe(III).[64] The increasing background in the high binding energy side is due to the O KLL Auger emission.[65]

The heat treatment significantly influences the Sr 3d peak position and shape (Figure 3, Table 3). The fitting procedure of the Sr 3d peak reveals three pairs of spin–orbit doublets which indicate that strontium exists in different chemical

(64) Glisenti, A.; Favero, G.; Granozzi, G. *J. Chem. Soc., Faraday Trans.* **1998**, *94*, 173.

Table 4. Nominal and XPS Compositions (atomic %) for All the $La_{0.6}Sr_{0.4}Co_{1-y}Fe_yO_{3-\delta}$ Powders Heated at 873 and 1073 K before and after H_2-TPR Experiment, Respectively

		XPS				XPS		
element	nominal	873 K	1073 K	1073 K H_2-TPR	nominal	873 K	1073 K	1073 K H_2-TPR
				$La_{0.6}Sr_{0.4}Co_{0.8}Fe_{0.2}O_{3-\delta}$				
La	14	10	10	10	30	28	28	34
Sr	9	5	7	9	20	14	20	32
Co	18	17	14	6	40	46	40	22
Fe	4	4	5	3	10	12	12	12
O	55	63	64	72				
				$La_{0.6}Sr_{0.4}Co_{0.5}Fe_{0.5}O_{3-\delta}$				
La	13	11	10	8	30	31	26	27
Sr	9	7	9	11	20	20	23	37
Co	11	9	10	4	25	25	27	15
Fe	11	9	9	6	25	24	24	21
O	56	64	62	71				
				$La_{0.6}Sr_{0.4}Co_{0.2}Fe_{0.8}O_{3-\delta}$				
La	13	9	7	6	30	26	20	22
Sr	9	11	12	12	20	31	35	43
Co	4	4	3	3	10	11	10	10
Fe	17	11	12	7	40	32	35	25
O	57	65	66	72				

environments. The Sr $3d_{5/2}$ contribution around 131.8−132.1 eV is characteristic of Sr(II) in perovskite phase,[56] the one around 133.2−133.7 eV is due to $SrCO_3$,[56,66] whereas the contribution at higher binding energy (around 133.8–135.8 eV) suggests the presence of SrO.[67] The comparison between the Sr 3d spectra obtained at 873 and 1073 K indicates that increasing the calcination temperature the contribution characteristic of strontium in perovskite phase becomes more evident, whereas the one due to strontium in SrO decreases. In particular, the decrease in this last contribution is particularly marked in the sample richer in iron. This behavior suggests that the strontium enters into perovskite structure at high temperature, confirming the XRD outcomes. The significant intensity of the component characteristic of the Sr 3d in $SrCO_3$, also after the calcination at 1073 K, could be ascribable to the strong tendency of strontium to interact with atmospheric carbon dioxide.[68]

The fitting procedure of the O 1s peak shows that oxygen exists in many chemical environments (Figure 3, Table 3). The first contribution, around 528.7–529.0 eV, agrees with the expected value for lattice oxygen in perovskite.[56] The contribution at slightly higher binding energy (around 529.3–529.6 eV) can be attributed to M−O (M = La, Co, Fe, Sr) in pure oxides.[56,64,67] The contributions at high binding energies are indicative of the presence of surface hydroxyl groups (531.4–531.5 eV) and carbonate species (532.1−533.0 eV), respectively.[56] The presence of this last species is also confirmed by the contribution around 289.4 eV on the C 1s XP peak. An other peak centered at 533.9 eV is also observed on the $La_{0.6}Sr_{0.4}Co_{0.2}Fe_{0.8}O_{3-\delta}$ powder treated at 873 K. According to many authors, this signal could be due to either chemisorbed dioxygen species[56] or chemisorbed water or oxygen-containing organic compounds present on the surface.[69] This contribution disappears after the treatment at 1073 K.

The heat treatment at 1073 K also causes a slight shift of the O 1s peak toward low binding energies. This is consistent with the increase of the contribution characteristic of the lattice oxygen in perovskite and the decrease of the signal due to M−O (M = La, Co, Fe, Sr) in pure oxides. The peak around 532.1−533.0 eV is still visible after the thermal treatment at high temperature, confirming the fast surface carbonatation of these powders.

The atomic compositions obtained from XPS analyses are summarized in Table 4. All the samples are particularly rich in oxygen with respect to the nominal composition. This result agrees with the already mentioned presence of hydroxyl and carbonate groups. For both the $La_{0.6}Sr_{0.4}Co_{0.8}Fe_{0.2}O_{3-\delta}$ and $La_{0.6}Sr_{0.4}Co_{0.5}Fe_{0.5}O_{3-\delta}$ samples, the amounts of the different cations are very similar to the nominal values, and they do not change with the increase of calcination temperature. On the contrary, in the sample characterized by higher iron content (except the cobalt percentage which does not change with temperature) lanthanum and iron percentages are always lower than the nominal values. The strontium amount instead considerably increases with respect to the nominal value suggesting the thermally induced surface segregation of Sr. This result agrees with the already mentioned presence of carbonate and oxide species.

The three samples calcined at 1073 K were selected for a more detailed investigation.

Thermal analysis was carried out both in nitrogen and air flow without significant differences. The TG spectra of the three powders calcined at 1073 K are compared in Figure 4. All the samples show a marked weight loss at high temperature (from 1000 to 1173 K) mainly ascribable to the decomposition of carbonate species, whose presence is also revealed by XRD and XPS analysis. This weight loss is 3.53, 3.16, and 2.16% respectively for $La_{0.6}Sr_{0.4}Co_{0.8}Fe_{0.2}O_{3-\delta}$, $La_{0.6}Sr_{0.4}Co_{0.5}Fe_{0.5}O_{3-\delta}$, and $La_{0.6}Sr_{0.4}Co_{0.2}Fe_{0.8}O_{3-\delta}$. A dif-

(65) Bocquet, A. E.; Fujimori, A.; Mizokawa, T.; Saitoh, T.; Namatame, H.; Suga, S.; Kimizuka, N.; Takeda, Y.; Takano, M. *Phys. Rev. B* **1992**, *45*, 1561.
(66) Sosulnikov, M. I.; Teterin, Y. A. *J. Electron Spectrosc. Relat. Phenom.* **1992**, *59*, 111.
(67) Van Doveren, H.; Verhoeven, J. A. T. *J. Electron Spectrosc. Relat. Phenom.* **1980**, *21*, 265.
(68) Schmidt, M. *Mater. Res. Bull.* **2002**, *37*, 2093.
(69) Shkerin, S. N.; Kuznetsov, M. V.; Kalashnikova, N. A. *Russ. J. Elecrochem.* **2003**, *39*, 591.

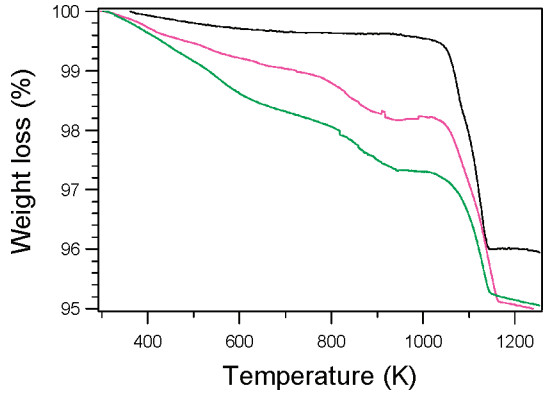

Figure 4. TG spectra (recorded in N_2) of the three $La_{0.6}Sr_{0.4}Co_{1-y}Fe_yO_{3-\delta}$ samples prepared by citrate gel method and treated at 1073 K: (black) $La_{0.6}Sr_{0.4}Co_{0.8}Fe_{0.2}O_{3-\delta}$; (magenta) $La_{0.6}Sr_{0.4}Co_{0.5}Fe_{0.5}O_{3-\delta}$; (green) $La_{0.6}Sr_{0.4}Co_{0.2}Fe_{0.8}O_{3-\delta}$.

ferent behavior is observed between RT and 1000 K: a quite weak and continuous weight loss due to water desorption and to condensation of hydroxyl groups characterizes the sample richer in cobalt ($La_{0.6}Sr_{0.4}Co_{0.8}Fe_{0.2}O_{3-\delta}$); as the iron amount increases, the weight losses become more intense.

The $La_{0.6}Sr_{0.4}Co_{1-y}Fe_yO_{3-\delta}$ samples show very low surface area, 4.1, 4.6, and 6.6 $m^2\ g^{-1}$ for $y = 0.2$, 0.5, and 0.8, respectively. These values agree with those obtained for similar compounds by Goldwasser et al.[21] and Bebel et al.[51] Moreover, in agreement with Bebel's observation,[51] a tendency to higher surface areas in going from $y = 0.2$ to $y = 0.8$ is observed.

The morphology of the materials calcined at 1073 K was investigated by SEM. Concerning the $La_{0.6}Sr_{0.4}Co_{0.8}Fe_{0.2}O_{3-\delta}$ sample, the scanning electron micrographs (Figure 5) reveal spherical particles which are clustered together, forming a highly porous microstructure composed by sheet-like fragments. The particles' diameters range from about 63 to 126 nm. The comparison of these data with the crystallite size calculated form the XRD spectra (Table 2) indicates that each particle is composed of many crystallites. Moreover, the SEM images reveal a homogeneous microstructure, which is confirmed by the homogeneous distribution of La, Sr, Co, and Fe revealed by the EDX microanalysis. It is remarkable to note that the grain-to-grain connectivity in the materials increases with the raise of iron content (Figures 6 and 7). $La_{0.6}Sr_{0.4}Co_{0.5}Fe_{0.5}O_{3-\delta}$ and, in particular, $La_{0.6}Sr_{0.4}Co_{0.2}Fe_{0.8}O_{3-\delta}$ show, due to the enhanced agglomeration, a more compact morphology. The particle diameter ranges from 61 to 104 nm in $La_{0.6}Sr_{0.4}Co_{0.5}Fe_{0.5}O_{3-\delta}$ and from 41 to 47 nm in $La_{0.6}Sr_{0.4}Co_{0.2}Fe_{0.8}O_{3-\delta}$. Smaller particles with a more and more narrow particle size distribution then characterize the samples with higher iron content, confirming the XRD outcomes. Moreover, it is noteworthy that the decrease in particle size with the increase of the Fe/Co atomic ratio correlates with the raise of the specific surface areas.

Figure 8 shows the temperature-programmed reduction (TPR) profiles recorded for the $La_{0.6}Sr_{0.4}Co_{1-y}Fe_yO_{3-\delta}$ materials after calcination at 1073 K. All the samples present complex TPR profiles composed of at least four reduction peaks, two of which are at low temperature while the others at high temperature. For the $La_{0.6}Sr_{0.4}Co_{0.8}Fe_{0.2}O_{3-\delta}$ sample,

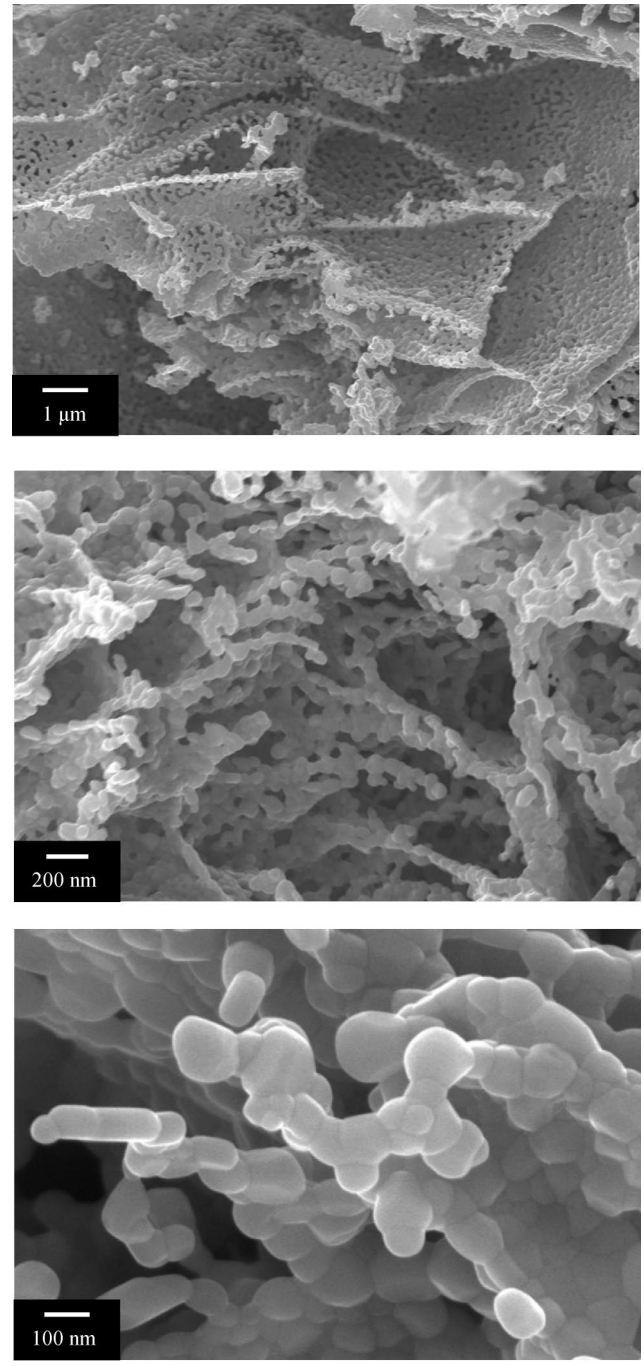

Figure 5. SEM micrographs of the $La_{0.6}Sr_{0.4}Co_{0.8}Fe_{0.2}O_{3-\delta}$ treated at 1073 K at different magnifications.

the peaks are centered at 630, 675, 1090, and 1225 K. A significant change in the relative intensity of the peaks at high temperature is observed for the $La_{0.6}Sr_{0.4}Co_{0.5}Fe_{0.5}O_{3-\delta}$ sample, whereas the other reduction peaks remain almost unperturbed. Finally, $La_{0.6}Sr_{0.4}Co_{0.2}Fe_{0.8}O_{3-\delta}$ shows a strong decrease of the intensity of the low-temperature processes, with a concomitant shift toward higher temperature of the whole reduction profile.

The complex redox behavior of Co and/or Fe-based perovskitic materials has not been fully clarified yet and various interpretations have been proposed. It was reported that $LaCoO_3$-based materials show two reduction processes

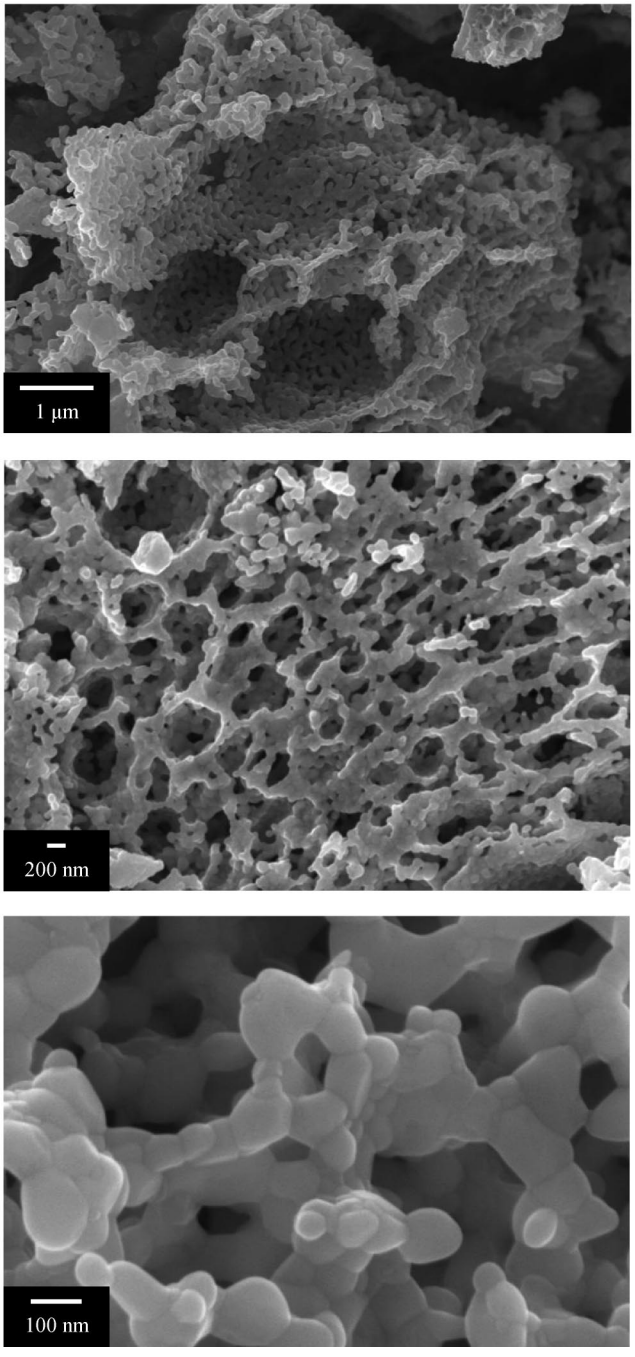

Figure 6. SEM micrographs of the $La_{0.6}Sr_{0.4}Co_{0.5}Fe_{0.5}O_{3-\delta}$ treated at 1073 K at different magnifications.

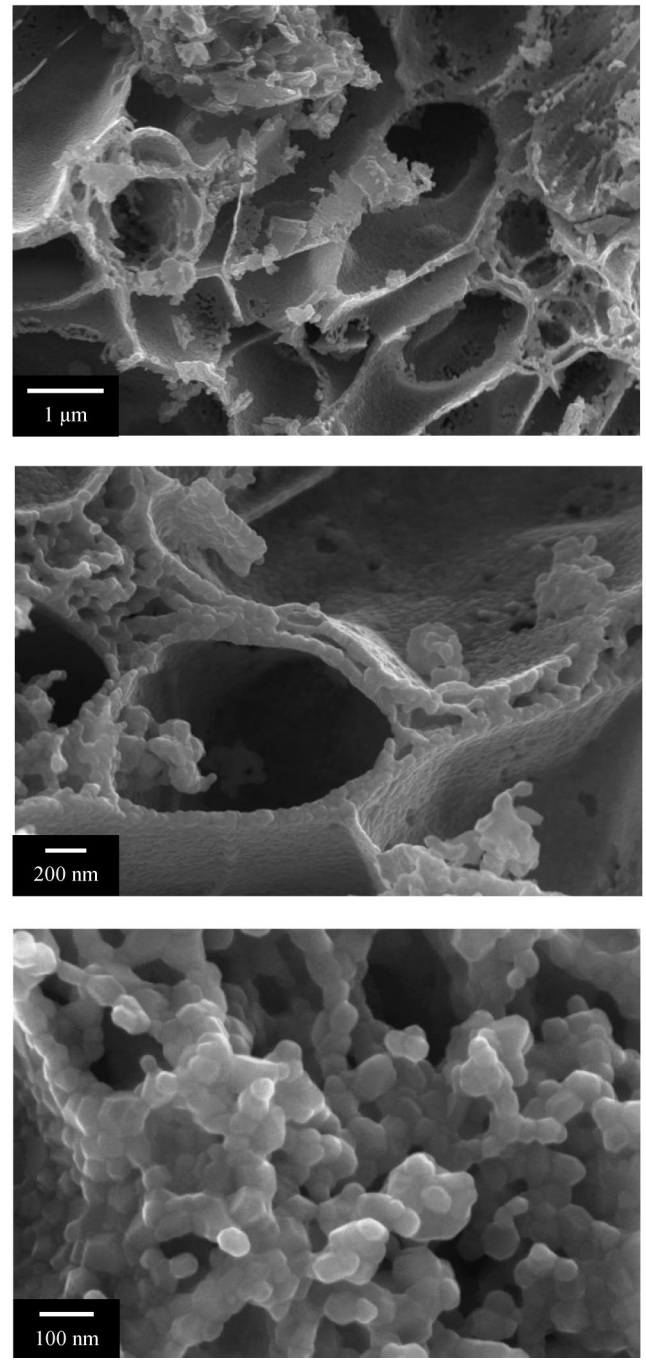

Figure 7. SEM micrographs of the $La_{0.6}Sr_{0.4}Co_{0.2}Fe_{0.8}O_{3-\delta}$ treated at 1073 K at different magnifications.

in the temperature range 673–973 K,[70,71] attributed to the reduction of Co(III) to Co(II) at low temperature and to the formation of Co(0) at high temperature, respectively. Moreover, Xiong et al.[72] attributed the different reduction peaks observed for Co_3O_4/Al_2O_3 catalysts to different cobalt species with different interaction with the support. Regarding the Fe-based materials, it was reported that reduction of Ca-doped $LaFeO_3$ occurs in the temperature range 500–750 K.[41] This process was attributed to the reduction of Fe(IV) to Fe(III). Above 900 K, the onset of a new reduction process was observed and attributed to the formation of Fe(0).[41] It is, thus, difficult to fully interpret the redox behavior of the present $La_{0.6}Sr_{0.4}Co_{1-y}Fe_yO_{3-\delta}$ materials. The non homogeneous nature of the samples contributes to complicate the interpretation: the concomitant reduction processes related to $LaSrCoO_4$, Co_3O_4, $LaSrFeO_4$, and Fe_2O_3 phases cannot be discarded (see below).

The TPR experiments suggest the presence of different amounts of reducible (and mobile) oxygen in the materials. It is worth noting that the increase of the iron content leads to a decrease of the amount of reducible oxygen at low temperature. This can have significant impact on the reactivity of these materials, especially in oxidation or reforming reaction involving lattice oxygen. Therefore the TPR data

(70) Royer, S.; Bérubé, F.; Kaliaguine, S. *Appl. Catal., A* **2005**, *282*, 273.
(71) Huang, L.; Bassir, M.; Kaliaguine, S. *Appl. Surf. Sci.* **2005**, *243*, 360.

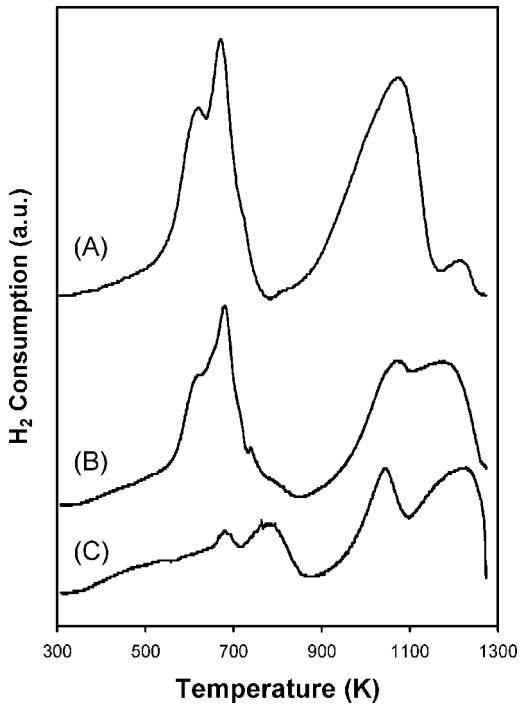

Figure 8. Temperature-programmed reduction (TPR) of the three $La_{0.6}Sr_{0.4}Co_{1-y}Fe_yO_{3-\delta}$ samples prepared by citrate gel method and treated at 1073 K: (A) $La_{0.6}Sr_{0.4}Co_{0.8}Fe_{0.2}O_{3-\delta}$; (B) $La_{0.6}Sr_{0.4}Co_{0.5}Fe_{0.5}O_{3-\delta}$; (C) $La_{0.6}Sr_{0.4}Co_{0.2}Fe_{0.8}O_{3-\delta}$.

suggest that the decrease in the iron content should favor alcohol reforming reaction (see below).

For a better comprehension of the TPR profiles, XRD and XPS measurements were performed on the three $La_{0.6}Sr_{0.4}Co_{1-y}Fe_yO_{3-\delta}$ samples after reduction at 873 K for 2 h.

As shown in Figure 1 (see dotted lines) and Table 1, the perovskite phase is always preserved after reduction as the main phase. The cell parameters of the perovskite phase do not significantly change after the H_2 reduction at 873 K, while a decrease of crystallite size is observed. Also the $SrCO_3$ phase is still observed on all the diffraction patterns. Moreover, its amount slightly increases. Concerning the sample characterized by higher cobalt content, besides weak signals of $SrLaCoO_4$, reflections of La_2CoO_4 and metallic cobalt (both cubic and hexagonal phases) are also detected after reduction. Instead, only weak signals of La_2CoO_4 and metallic cobalt are evident, in addition to the reflections of the initial perovskite and $SrCO_3$, in the diffractogram recorded after reduction on the sample with $y = 0.5$. The analysis of the XRD spectrum of the sample characterized by higher iron content reveals that the reduction at 873 K causes a significant decrease of the weight fraction of the $SrLaFeO_4$ phase, the disappearance of the Fe_2O_3 phase and the formation of metallic iron. From Table 1, it is evident that the reduction affects mostly the secondary phases: $SrLaCoO_4$ and Co_3O_4 for the samples with $y = 0.2$, 0.5 and $SrLaFeO_4$ and Fe_2O_3 for the samples with $y = 0.8$. Nakamura et al.[73] reported that the decomposition of $LaCoO_3$-based perovskite in reducing atmosphere includes several stages: formation of cobalt oxides and La_2CoO_4; then the cobalt cations are further reduced to Co(0) and La_2O_3 is formed.

As a general consideration, the above results show that the perovskite phase is rather stable even after an aggressive treatment as a reduction with H_2 (5%)/Ar flow at high temperature. These results are in agreement with findings of Merino et al.[74] Moreover, they reported that incorporation of iron enhances the structural stability of $LaCoO_3$-based perovskite.

XP spectra recorded after reduction with H_2 (5%)/Ar at 873 K (dotted lines in Figures 2 and 3) reveal several changes on the samples surface. The slight increase in the lanthanum XP peak fwhm (full width at half maximum) and its shift toward higher BE (Figure 2) suggest the formation of lanthanum oxide and mostly hydroxide. This is particularly evident on the sample richer in cobalt. The significant formation of hydroxyl species is also confirmed by the marked increase of the contribution around 531.4 eV (characteristic of hydroxyl groups) on the O 1s XP peak (Figure 3). A careful analysis of the intensity of the peak at 531.4 eV confirms that the surface hydroxylation lowers with the raise of the iron content consistently with the above-mentioned La 3d peak shape evolution. The formation of lanthanum oxide and hydroxide is in agreement with the reduction conditions and the above-mentioned decomposition mechanism of the lanthanum-containing compounds, which shows the formation of La_2O_3 in association with Co(0) nanoparticles. These results reveal that the surface of the reduced samples are characterized by a higher heterogeneity than the as-prepared catalysts.

The shape of the Sr 3d peak (Figure 3) also changes as a consequence of the reduction treatment. The comparison with the XP spectra recorded on the as prepared catalyst (unreduced) reveals a decrease in the Sr $3d_{5/2}$ contribution characteristic of Sr(II) in perovskite phase (around 131.8 eV) and a slight increase in the one due to Sr(II) in SrO (at higher BE). SrO can be a product of the decomposition of perovskite, $SrLaCoO_4$ and $SrLaFeO_4$ phases. As already asserted, however, the reduction concerns mostly the last two species. The above-mentioned trend is particularly evident on the $La_{0.6}Sr_{0.4}Co_{0.8}Fe_{0.2}O_{3-\delta}$ and $La_{0.6}Sr_{0.4}Co_{0.5}Fe_{0.5}O_{3-\delta}$ materials.

Concerning the Co 2p XP peak (Figure 2), the core level binding energies do not change as a consequence of the reduction treatment. However, some relevant changes of peak shape are evident. The weak increase of the shake-up contributions on the spectrum of the sample with higher Co/Fe atomic ratio confirms a weak reduction of Co(III) to Co(II). Instead, the slight widening toward low binding energies of Co 2p peak of the samples with higher cobalt amount allows to consider the possible presence of Co(0).[61,62]

As a general consideration, the reduction treatment under H_2 (5%)/Ar flow at 873 K does not modify the Fe 2p peak shape and positions (Figure 2). However, in the sample with higher iron content the slight broadening of the Fe 2p peak

(72) Xiong, H.; Zhang, Y.; Wang, S.; Li, J. *Catal. Commun.* **2005**, *6*, 512.
(73) Nakamura, T.; Petzow, G.; Gauckler, L. J. *Mater. Res. Bull.,* **1979**, *14*, 649.
(74) Merino, N. A.; Barbero, B. P.; Ruiz, P.; Cadús, L. E. *J. Catal.* **2006**, *240*, 245.

toward low binding energy suggests the presence of iron in lower oxidation state.[75]

The atomic surface compositions obtained from XPS after the reduction treatment are reported in Table 4. The comparison of the oxygen amounts before and after the reduction treatment confirms the strong surface oxygen enrichment. Concerning the cations, the lanthanum amount does not change significantly as a consequence of the reduction treatment, suggesting that mainly a redistribution of the lanthanum cations in different chemical environment occurs. The strontium percentage is higher than the nominal composition and the unreduced XPS values indicating that the reduction treatment causes a strong strontium segregation. The reduction treatment causes the decrease of the cobalt amount. This behavior becomes more and more evident with the increase in the Co/Fe atomic ratio. A similar behavior can be observed for iron with the decrease in the Co/Fe atomic ratio.

On the basis of the XRD and XPS characterization, it is possible to conclude that the reduction treatment at 873 K affects mainly the secondary phases, maintaining unperturbed the major perovskitic phase. The reduction of the materials results in the strontium segregation on the surface, in a major extent with the increase of the iron content, and in the formation of Co(0) and/or Fe(0) nanoparticles, depending on the initial composition of the material.

(b) Catalytic Activity. *Methanol Steam Reforming.* Figure 9 shows the results of the steam reforming of methanol over $La_{0.6}Sr_{0.4}Co_{1-y}Fe_yO_{3-\delta}$ after cleaning in flowing O_2(5%)/Ar. The ability to catalyze the decomposition and/or reforming of methanol is promoted by increasing the Co/Fe atomic ratio. In fact, the light-off temperatures (corresponding to 50% of methanol conversion) are 640, 655, and 695 K for $y = 0.2$, 0.5, and 0.8, respectively. Moreover, the complete methanol conversion is reached at 705, 715, and 815 K, respectively.

The composition of the perovskitic material also influences the product distribution. Increasing the Co/Fe atomic ratio, the decomposition/reforming of methanol reactions are promoted and the water gas shift reaction reaches the thermodynamic equilibrium at lower temperatures. No formaldehyde production is observed during the run-up experiments on the various samples. On the $La_{0.6}Sr_{0.4}Co_{0.2}Fe_{0.8}O_{3-\delta}$ material significant amount of CH_4 is observed, as a product of the hydrogenation of CO and CO_2. This parallel reaction decreases the H_2 yield and produces an undesired byproduct. No methane formation is observed using the materials with minor iron content ($y = 0.5$ and 0.2). The CH_4 production can be clearly attributed to the high iron content. In fact, Co/Fe catalysts are widely studied in the Fischer–Tropsch synthesis starting from $H_2/CO/CO_2$ mixtures and it is reported that increasing the iron content a significant modification of the selectivity is observed toward the formation of lighter fraction.[76] Moreover, it has been

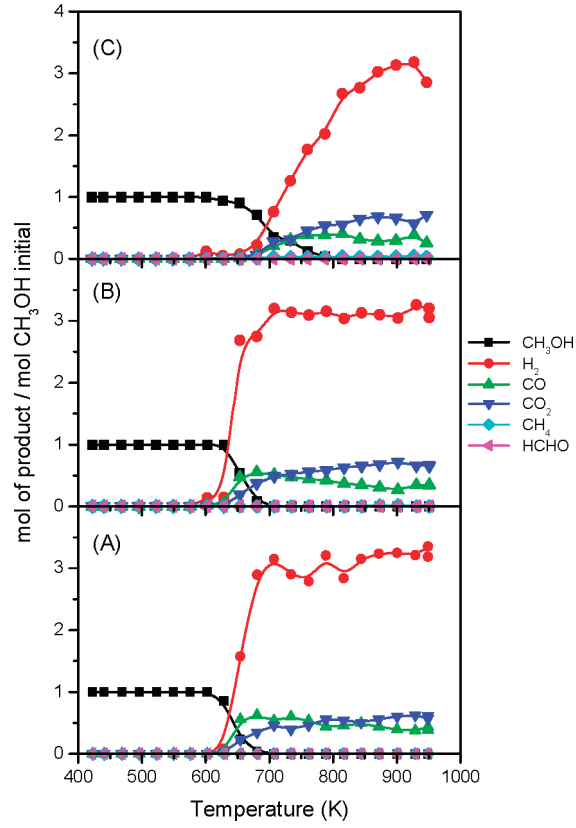

Figure 9. Catalytic activity profiles of the $La_{0.6}Sr_{0.4}Co_{1-y}Fe_yO_{3-\delta}$ samples toward methanol steam reforming, after standard cleaning of the samples in O_2 (5%)/Ar at 773 K for 1 h: (A) $La_{0.6}Sr_{0.4}Co_{0.8}Fe_{0.2}O_{3-\delta}$; (B) $La_{0.6}Sr_{0.4}Co_{0.5}Fe_{0.5}O_{3-\delta}$; (C) $La_{0.6}Sr_{0.4}Co_{0.2}Fe_{0.8}O_{3-\delta}$.

recently reported that it is possible to increase significantly the CO hydrogenation activity of nickel catalysts by alloying with iron.[77]

No significant deactivation of the catalyst activity is observed in consecutive run-up experiments.

It is worth noting that a prereduction treatment at 873 K in flowing H_2 (5%)/Ar at 873 K induces only minor modification of the activity.

The obtained results suggest that $La_{0.6}Sr_{0.4}Co_{1-y}Fe_yO_{3-\delta}$ materials possess a good catalytic activity with respect to the dehydrogenation of alcohols, in particular when the Co/Fe molar ratio is higher than 1. For the material with the higher iron content, a significant hydrogenation reaction occurs.

Ethanol Steam Reforming. The steam reforming of ethanol is a reaction extensively studied over a wide range of heterogeneous catalysts.[78–83] The mechanism of the reaction involves a complex network of reactions, as suggested by Fatsikostas et al.[78] and Frusteri et al.[79] The ethanol conversion can occur through two parallel reaction pathways,

(75) McIntyre, N. S.; Zetaruk, D. G. *Anal. Chem.* **1977**, *49*, 1521.
(76) de la Péna O'Shea, V. A.; Menéndez, N. N.; Tornero, J. D.; Fierro, J. L. G. *Catal. Lett.* **2003**, *88*, 123.
(77) Kustov, A. L.; Frey, A. M.; Larsen, K. E.; Johannessen, T.; Nørskov, J. K.; Christensen, C. H. *Appl. Catal., A* **2007**, *320*, 98.
(78) Fatsikostas, A. N.; Verykios, X. E. *J. Catal.* **2004**, *225*, 439.
(79) Frusteri, S.; Freni, S.; Spadaro, L.; Chiodo, V.; Bonura, G.; Donato, S.; Cavallaro, S. *Catal. Commun.* **2004**, *5*, 611.
(80) Homs, N.; Llorca, J.; de la Picina, P. R. *Catal. Today* **2006**, *116*, 361.
(81) Casanovas, A.; Llorca, J.; Homs, N.; Fierro, J. L. G.; de la Piscina, P. R. *J. Mol. Catal. A:Chem.* **2006**, *250*, 44.
(82) Breen, J. P.; Burch, R.; Coleman, H. M. *Appl. Catal., B* **2002**, *39*, 65.
(83) Montini, T.; De Rogatis, L.; Gombac, V.; Fornasiero, P.; Graziani, M. *Appl. Catal., B* **2007**, *71*, 125.

depending on the nature of the support. Ethanol is dehydrated to ethylene, which is subsequently converted to syngas over the metallic phase. This pathway is mainly promoted by acidic sites.[84,85] Deactivation of the catalysts during the reforming processes is usually attributed to coke deposition as a result of the production of large amounts of ethylene. On the other hand, ethanol could be converted to acetaldehyde through dehydrogenation.[86] The product is sequentially decomposed and converted into syngas over the metallic phase.

Besides ethylene and syngas, the reforming of ethanol could lead to the formation of acetone, accompanied by almost stoichiometric amounts of CO_2 and H_2. The conversion of ethanol into acetone was reported for Cu/CeO_2 catalysts[87,88] and has been recently observed on Rh nanoparticles embedded into a $Ce_XZr_{1-X}O_2-Al_2O_3$ matrix.[83] The formation of acetone proceeds through the dehydrogenation of ethanol to acetaldehyde, the aldol condensation to 3-hydroxybutanal, its oxidation to 3-hydroxybutirrate using the oxygen provided by the catalyst, and finally, the thermal decarbossilation and dehydrogenation of this product. Lattice oxygen involved in the first oxidative step can be restored by reaction with H_2O. The overall reaction can be expressed as

$$2CH_3CH_2OH + H_2O \rightarrow CH_3COCH_3 + CO_2 + 4H_2$$

Moreover, Nishiguchi et al.[88] demonstrated the importance of the presence of basic oxides (such as MgO) to favor this process, promoting the aldol condensation of acetaldehyde.

The steam reforming of ethanol was investigated on the $La_{0.6}Sr_{0.4}Co_{0.5}Fe_{0.5}O_{3-\delta}$ sample after different activation pretreatments (Figure 10).

The $La_{0.6}Sr_{0.4}Co_{0.5}Fe_{0.5}O_{3-\delta}$ material subjected to a cleaning treatment (Figure 10, part A) presents a significant ethanol conversion above 600 K. The major products observed up to 750 K are acetone, CO_2, and H_2 (maximum yield of acetone, 42% at 750 K). When the temperature is increased, significant amounts of acetaldehyde (maximum yields of 19% at 800 K) and ethylene (maximum yields of 22% at 825 K) are produced. Considerably, reforming product are observed above 825 K, whereas only above 900 K is ethanol completely converted into syngas. No significant deactivation is observed in the ethanol conversion during subsequent run-up experiments, although ethylene formation at intermediate temperatures is strongly reduced.

The sample subjected to a reduction treatment at 873 K (Figure 10B) shows a different distribution of products in the medium temperature range (600–900 K). In fact, the reduction treatment strongly reduces the ethylene formation and favors the acetone production at lower temperatures and the complete conversion of ethanol to syngas at high temperature (possible already at 870 K). No significant changes are observed in subsequent run-up experiments.

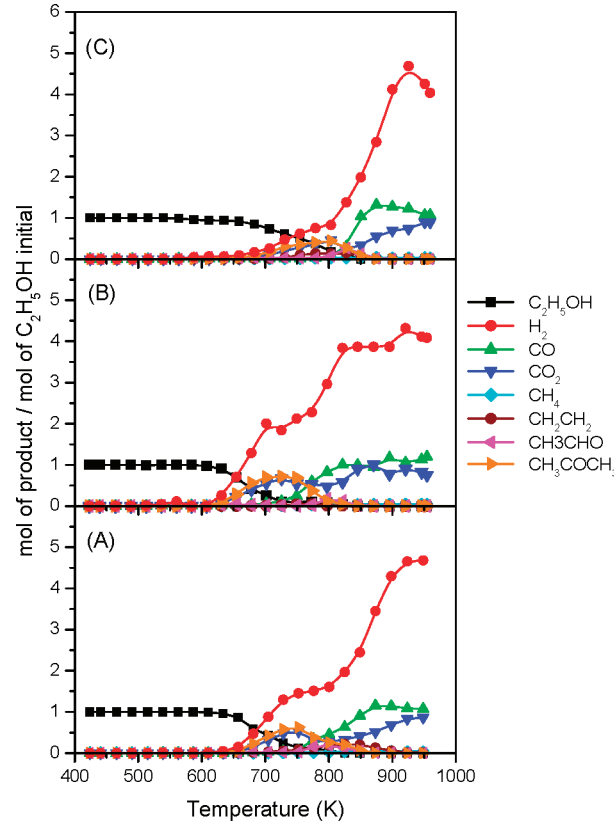

Figure 10. Catalytic activity profiles of the $La_{0.6}Sr_{0.4}Co_{0.5}Fe_{0.5}O_{3-\delta}$ toward ethanol steam reforming after different pretreatments: (A) cleaning in O_2 (5%)/Ar at 773 K for 1 h; (B) cleaning + reduction in H_2 (5%)/Ar at 873 K for 2 h; (C) cleaning + reduction in H_2 (5%)/Ar at 1273 K for 2 h.

The more severe reduction treatment (1273 K) deactivates the catalytic properties of the materials (Figure 10C): the conversion of ethanol moves to higher temperature and a complex mixture of products is formed up to 900 K. This deactivation effect can be associated with the sintering induced by the severe thermal aging. No further deactivation is observed in subsequent experiments.

The differences in the activity of the $La_{0.6}Sr_{0.4}Co_{0.5}Fe_{0.5}O_{3-\delta}$ sample after various reductive treatment can be rationalized in terms of the effect of the reduction temperature on the catalyst. In fact the steam reforming activity can be related essentially with the metal nanoparticles formed during the reduction. The sample subjected only to the cleaning presents low activity until 800 K producing acetone and ethylene. The ethanol conversion raises rapidly above 800 K (when metal nanoparticles could be formed by reduction of the material in the reaction mixture), leading to high reforming activity. After reduction at 873 K, well-dispersed Co(0) nanoparticles are formed (see XRD analysis) that favor the dehydrogenation of ethanol leading to acetone formation in the medium temperature range (600–800 K). On the other hand, after reduction at 1273 K, it is reasonable to suppose that Co(0) nanoparticles could be deep sintered, reducing the active surface for the ethanol conversion and shifting the activity at higher temperature.

In the medium temperature range (600–800 K), a high selectivity to acetone is observed. In this temperature range, in fact, the $La_{0.6}Sr_{0.4}Co_{0.5}Fe_{0.5}O_{3-\delta}$ material, as already shown in the case of methanol conversion (see above), possesses a

(84) Phillips, C. B.; Datta, R. *Ind. Eng. Chem. Res.* **1997**, *36*, 4466.
(85) Zaki, T. *J. Colloid Interface Sci.* **2005**, *284*, 606.
(86) Rosini, C.; Cavallaro, S.; Frusteri, F.; Freni, S.; Busca, G. *React. Kinet. Catal. Lett.* **2007**, *90*, 117.
(87) Elliott, D. J.; Pennella, F. *J. Catal.* **1989**, *119*, 359.
(88) Nishiguchi, T.; Matsumoto, T.; Kanai, H.; Utani, K.; Matsumura, Y.; Shen, W.-J.; Imamura, S. *Appl. Catal., A* **2005**, *279*, 273.

good dehydrogenation ability. Moreover, the aldol condensation (second step of the acetone formation) can be promoted by the basic sites exposed on the catalyst surface. These could be related both to the perovskite phases and to minor amounts of La_2O_3 and/or SrO, segregated on the surface (see XPS characterization). Finally, the oxidative step can be favored by the redox mechanisms related to the perovskite phases. Notably, for the $La_{0.6}Sr_{0.4}Co_{0.5}Fe_{0.5}O_{3-\delta}$ material after reduction at 873 K the selectivity to acetone formation approaches 100% around 750 K, indicating that this kind of material could be useful for the conversion of ethanol to this widely used compound.

The production of ethylene from dehydration of ethanol is usually associated with the reactivity of the acidic sites of the catalysts. In the case of the $La_{0.6}Sr_{0.4}Co_{0.5}Fe_{0.5}O_{3-\delta}$ material, the more acidic sites present on the surface of the catalyst should be the cations hosted in the B-site of the perovskite (Co and/or Fe) in their higher oxidation state. In fact, the cleaned sample (Figure 10A) shows the higher yield to ethylene (22% at 825 K). Consistently, the ethylene production is almost suppressed after reduction at 873 K (Figure 10B). This result could be due to a lower acidity of the surface or to the competition of the dehydrogenation reaction promoted by the Co(0) nanoparticles formed during the reduction. Consistently, in the second run-up experiment on the cleaned sample (data not shown), the ethylene production is strongly minimized as a result of the reduction of the material in the reaction mixture during the first run-up experiment.

Figure 11 shows the effect of the Co/Fe atomic ratio on the catalytic activity in the steam reforming of ethanol of the $La_{0.6}Sr_{0.4}Co_{1-y}Fe_yO_{3-\delta}$ samples after cleaning and reduction at 873 K. The obtained results suggest that the Co/Fe atomic ratio strongly influences the activity of the materials. In fact, the $La_{0.6}Sr_{0.4}Co_{0.8}Fe_{0.2}O_{3-\delta}$ material presents a light-off temperature for ethanol conversion of 755 K and complete conversion is reached only above 925 K. On the other hand, the $La_{0.6}Sr_{0.4}Co_{0.2}Fe_{0.8}O_{3-\delta}$ sample presents an on-set of ethanol conversion at the same temperature of $La_{0.6}Sr_{0.4}Co_{0.5}Fe_{0.5}O_{3-\delta}$ but a plateau is observed around the light-off temperature and the following part of the ethanol conversion is shifted to higher temperature. Moreover, both the materials present high production of ethylene and acetaldehyde in the medium−high temperature range and reach the maximum of the H_2 yield only at higher temperature with respect to the material with $y = 0.5$.

The differences between the activity of the $La_{0.6}Sr_{0.4}Co_{0.5}Fe_{0.5}O_{3-\delta}$ with respect to the other samples suggest that the Co/Fe atomic ratio of 1 is the best compromise to obtain good performance in the ethanol steam reforming activity.

With the lower Co/Fe atomic ratio ($La_{0.6}Sr_{0.4}Co_{0.2}Fe_{0.8}O_{3-\delta}$ sample), XRD shows the formation of Fe(0) nanoparticles. In this sample, the amount of Co(0) can be reasonable not enough to obtain a good conversion/activity at low temperature. Moreover, the activity of Fe(0) and Co(0) nanoparticles could be different: although it is known that Co(0) is active for the steam reforming of ethanol,[89–91] no indication are reported in the literature (at the actual knowledge of the authors) regarding the activity of Fe(0) nanoparticles under the reaction conditions employed in this study.

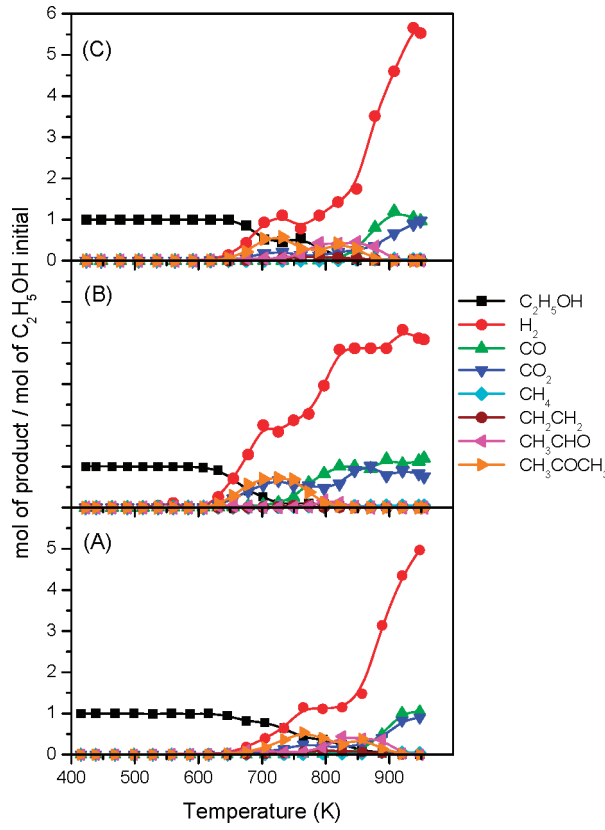

Figure 11. Catalytic activity profiles of the $La_{0.6}Sr_{0.4}Co_{1-y}Fe_yO_{3-\delta}$ samples toward ethanol steam reforming, after standard cleaning of the samples in O_2 (5%)/Ar at 773 K for 1 h followed by reduction in flowing H_2 (5%)/Ar at 873 K for 1 h: (A) $La_{0.6}Sr_{0.4}Co_{0.8}Fe_{0.2}O_{3-\delta}$; (B) $La_{0.6}Sr_{0.4}Co_{0.5}Fe_{0.5}O_{3-\delta}$; (C) $La_{0.6}Sr_{0.4}Co_{0.2}Fe_{0.8}O_{3-\delta}$.

On the other hand, with the higher Co/Fe atomic ratio ($La_{0.6}Sr_{0.4}Co_{0.8}Fe_{0.2}O_{3-\delta}$ sample), a large number of Co(0) nanoparticles form on the surface and their sintering could be possible also at low temperature. It is known that the dimension of Co(0) nanoparticles has a strong influence in the ability of adsorption and activation of ethanol under steam reforming conditions.[91] The reduction of the metallic surface area could be the reason for the lower activity of this material in the reforming of ethanol. Moreover, a different activity between the nanoparticles with hcp and ccp structure can not be excluded.

Conclusions

$La_{0.6}Sr_{0.4}Co_{1-y}Fe_yO_{3-\delta}$ ($y = 0.2$, 0.5, 0.8) powders were prepared by the citrate gel method in order to investigate the influence of cobalt/iron ratio on the properties as well as on the catalytic activity.

It is worth underline that the substitution of iron for cobalt leads to several important structural, morphological, physical, and chemical changes. Perovskite structure is the main phase for all of the samples studied. As a matter of fact, with

(89) Kaddouri, A.; Mazzocchia, C. *Catal. Commun.* **2004**, *5*, 339.
(90) Llorca, J.; Homs, N.; de la Piscina, P. R. *J. Catal.* **2004**, *227*, 556.
(91) Haga, F.; Nakajima, T.; Yamashita, K.; Mashima, S. *React. Kinet. Catal. Lett.* **1998**, *63*, 253.

increasing of the iron amount the perovskite structure changes from rhombohedral ($y < 0.5$) to orthorhombic ($y > 0.5$). Moreover, substituting iron for cobalt a decrease of the average crystallite size is observed and consequently a raise of the specific surface area. Because of the enhanced agglomeration, the perovskites with higher amounts of iron show a more compact morphology. All the perovskite phases are rather stable even after such an aggressive treatment as reduction with H_2 (5%)/Ar flow at high temperature.

All the samples present a significant catalytic activity toward methanol steam reforming with a good selectivity to H_2 over the whole range of temperatures. The ability to catalyze the decomposition and/or reforming of methanol is promoted by increasing the Co/Fe ratio. In the steam reforming of ethanol, the $La_{0.6}Sr_{0.4}Co_{0.5}Fe_{0.5}O_{3-\delta}$ presents the better performance, especially after reduction at 873 K, with the complete conversion of ethanol into syngas above 850 K and the almost complete suppression of the ethylene formation at lower temperature.

Finally, no significant deactivation of the catalyst activity is observed in consecutive run-up experiments.

Acknowledgment. The authors gratefully acknowledge Prof. E. Tondello (University of Padova) and Prof. M. Graziani (University of Trieste) for helpful discussions, Dr L. Lutterotti (University of Trento) for helpful support in XRD data refinement, and Dr C. Maccato (University of Padova) for SEM analysis. This work was supported by the following research programs: Progetto di Ateneo "Nuovi sistemi nanocompositi come materiali attivi in celle a combustibile ad ossido solido", FISR-MIUR "Nanosistemi inorganici ed ibridi per lo sviluppo e l'innovazione di celle a combustibile", University of Padova, University of Trieste, INSTM, and CENMAT.

Supporting Information Available: Rietveld refinement of XRD patterns recorded on the $La_{0.6}Sr_{0.4}Co_{0.8}Fe_{0.2}O_{3-\delta}$ sample treated at 1073 K before and after H_2-TPR experiment and fitting of Sr 3d and O 1s XP peaks of $La_{0.6}Sr_{0.4}Co_{0.8}Fe_{0.2}O_{3-\delta}$ (PDF). This material is available free of charge via the Internet at http://pubs.acs.org.

CM703329K